Journal of Materials Chemistry A

ROYAL SOCIETY OF CHEMISTRY

PAPER

View Article Online
View Journal | View Issue





Cite this: *J. Mater. Chem. A*, 2020, **8**, 12106

# A three-dimensional nitrogen-doped graphene framework decorated with an atomic layer deposited ultrathin $V_2O_5$ layer for lithium sulfur batteries with high sulfur loading†

Xiaowei Liu,[a] Zhaohuai Li,[a] Xiaobin Liao,[b] Xufeng Hong,[a] Yan Li,[b] Cheng Zhou,[a] Yan Zhao,[b] Xu Xu*[a] and Liqiang Mai*[a]

Received 23rd April 2020
Accepted 25th May 2020

DOI: 10.1039/d0ta04301j

rsc.li/materials-a

Lithium–sulfur batteries with ultra-high theoretical capacity have gradually become candidates to replace existing energy systems. However, the severe polysulfide shuttle effect hinders their commercialization process. Although using polar materials to modify the electrode for the adsorption of lithium polysulfides (LiPSs) can improve the cycle stability to a certain extent, it also causes the decline of the overall energy density due to the extra mass. Herein, we decorate three-dimensional nitrogen-doped graphene (3DNG) with ultra-thin $V_2O_5$ coatings (ALDVO@3DNG) on interior surfaces *via* controllable atomic layer deposition (ALD). The large number of chemisorption sites can firmly anchor LIPSs and inhibit the shuttle effect, while its ultrathin thickness allows the smooth transfer of electrons and promotes the conversion of polysulfides. As a consequence, by controlling the cycles of the ALD process, the optimized ALDVO@3DNG composite delivers an exceptionally great first-cycle discharge capacity of 1555 mA h $g^{-1}$ at 0.2C, despite the poor conductivity of $V_2O_5$. And it exhibits a good cycling stability with an average decay rate of 0.052% at 2C. Even with a high sulfur loading up to 11.5 mg $cm^{-2}$, the ALDVO@3DNG composite still reaches a great capacity of 1296 mA h $g^{-1}$ (corresponding to an areal capacity of 14.9 mA h $cm^{-2}$). This work provides an idea and experimental exploration of applying ALD for the ultrathin modification layer to enhance the electrochemical properties with a low extra weight burden, which may extend to other materials that may be applied in Li–S batteries.

## 1. Introduction

As the current commercial energy storage devices cannot keep step with the growing requirement for personal electronics and electric vehicles, many researchers regard lithium–sulfur (Li–S) batteries as a quite promising candidate for replacing current energy systems, because they can provide a higher theoretical capacity (1675 mA h $g^{-1}$) and energy density (2600 W h $kg^{-1}$) than the common lithium-ion batteries (LiBs).[1,2] Furthermore, their rich reserves, non-toxicity, environmental benignity and economic cost make lithium–sulfur batteries favorable to the large-scale implementation of devices.[3,4] However, there still exist several knotty issues stopping Li–S batteries from commercialization, including the insulating nature of S and $Li_2S$ and huge volume change (about 80%) when sulfur is converted to $Li_2S$, which can result in the breakdown of the electrode structure.[5–8] And most importantly, the S based cathode has a severe shuttling effect that the soluble lithium polysulfides (LiPSs, $Li_2S_x$, $4 \leq x \leq 8$) generated in the cathode pass through the separator, and then shift to the anode because of the concentration difference and form solid short-chain LiPSs on the anode surface, resulting in the wastage of sulfur and the passivation of the anode surface, eventually leading to a worse coulombic efficiency and rapid capacity fading.[9–12]

In the past few decades, in order to solve the problems mentioned above, extensive efforts have been devoted to constructing various progressive carbonaceous carrier materials as stable cathodes to load sulfur, such as hierarchical graphene composites and carbon nanotubes.[13–16] Under these circumstances, self-supported carbon-based cathodes have been turned into the most popular matrices for Li–S batteries, because they can meet the requirement of excellent mechanical integrity and superior electronic conductivity which is derived from the non-conducting polymer binder-free construction.[17,18] These properties can shorten the diffusion paths for both ionic

[a]State Key Laboratory of Advanced Technology for Materials Synthesis and Processing, International School of Materials Science and Engineering, Wuhan University of Technology, Wuhan 430070, Hubei, China. E-mail: xuxu@whut.edu.cn; mlq518@whut.edu.cn

[b]State Key Laboratory of Silicate Materials for Architectures, International School of Materials Science and Engineering, Wuhan University of Technology, Wuhan 430070, Hubei, China

† Electronic supplementary information (ESI) available: X-ray diffraction, cyclic voltammetry, and morphological characterization. See DOI: 10.1039/d0ta04301j

and electrical transport; in the meanwhile, large internal space can effectively cushion the S volume expansion, meanwhile providing more electrode–electrolyte contact area.[19–22]

Though these carbonaceous structures can obviously improve the cathode performance of Li–S batteries, there still exist tough difficulties to amend practical Li–S batteries in both stable capacity retention rate and rate capability. As is well known, carbonaceous cathodes are non-polar materials, which means the chemical bonding forces between the polar hydrophilic lithium polysulfides and carbonaceous host are relatively weak. The inhibition of the severe shuttling effect in these studies is mainly realized by utilizing physical encapsulation, resulting in the loose limitation of intermediate polysulfides.[23,24] Thus, chemical adsorption with more powerful force is necessary in avoiding the dissolution of LiPSs to prolong the cycle life of Li–S batteries. Under this background, researchers have paid much attention to metal oxides, which have been proved to be an effective chemical adsorbent for trapping the soluble LiPSs.[10,25–31] The Cai group reported a nitrogen-enriched mesoporous carbons/$La_2O_3$/S nanocomposite as a cathode possessing a nice capacity of 1043 mA h $g^{-1}$ at 1C to restrain LiPSs from dissolving in the electrolyte,[32] which retained a good cycling stability. The Lou group[33] designed a sulfur host decorated with TiO@C hollow nanospheres exhibiting excellent cycle performance with an average attenuation rate of 0.08% per cycle at 0.5C during a long-term circulation test, which was mainly due to the strong chemical force between TiO@C hollow nanospheres and LiPSs. Unfortunately, most methods in these studies applying wet chemical synthesis to get a metal oxide/carbon/S composite cathode could hardly control morphologies with uniform particle sizes and close connection between two components.

Compared to wet chemical methods, the atomic layer deposition (ALD) technology is gradually applied in cathode modification of Li–S batteries, as it has conformal surface decoration with a highly precise thickness controllability at the atomic scale.[34,35] In recent years, many metal oxide coatings have been applied in Li–S systems by ALD, which successfully worked in enhancing carbonaceous cathodes,[36–38] separators[39] and lithium metal anodes.[40] Wang and co-workers[41] utilized ALD to modify a graphene matrix with $TiO_2$. It offered a first-cycle capacity of 1070 mA h $g^{-1}$ at 1C and retained 918.3 mA h $g^{-1}$ after 500 cycles. However, also as a good absorbent, $V_2O_5$ with a stronger chemical interaction with LiPSs than $TiO_2$, is rarely reported because of its poor electrical conductivity. The commonly synthesized $V_2O_5$ with a size of hundreds of nanometers or even at the micrometer level will slow down the electron transport speed and interrupt the ion diffusion process, and lead to inferior electrochemical performance. Cary L. Pint and co-workers[42] deposited $V_2O_5$ on a carbon nanotube as the sulfur host through the ALD method to obtain an electrode with good cycling performance. However, the discharge capacity is relatively low and the rate performance is unsatisfactory and even the areal sulfur loading is not a high value of 1.5 mg $cm^{-2}$.

Herein, so as to utilize this decent absorbent effectively, we decorated a three-dimensional nitrogen-doped graphene (3DNG) matrix with ultrathin and uniform $V_2O_5$ layers *via* the ALD technique to serve as a cathode. The 3DNG cathode for Li–S batteries that contained neither conductive additives nor binders was fabricated by the hydrothermal self-assembly method and able to provide superb electron and ion transport pathways. Moreover, the cross-linking micron-sized void structure can effectively inhibit the volume expansion when sulfur is converted to $Li_2S$. Then $V_2O_5$ layers *via* the ALD process were uniformly covered on the internal surfaces of 3DNG with an inappreciable additional weight to prevent the reduction of the integral gravimetric capacity of the entire Li–S batteries. As chemisorption is monolayer adsorption, uniformly covered $V_2O_5$ layers of several nanometers will have little impact on the conductivity of the entire material system, and can theoretically work well for anchoring soluble LiPSs during charge and discharge at the same time. As a consequence, the ALDVO@3DNG electrode exhibited excellent initial capacity of 1256 mA h $g^{-1}$ at 0.5C, while it could still retain a capacity of 1113 mA h $g^{-1}$ after 100 cycles. Furthermore, at a high current density of 3C, it also exhibited a splendid capacity of 466 mA h $g^{-1}$. And we also successfully made a cathode with a really high areal sulfur loading of 11.5 mg $cm^{-2}$ and a great initial capacity of 1296 mA h $g^{-1}$ (corresponding to an areal capacity of 14.9 mA h $cm^{-2}$), demonstrating that the ALDVO@3DNG composite possessed superior electrochemical properties.

## 2. Experimental section

### 2.1 Preparation of the 3DNG aerogel

A graphene oxide (GO) aqueous dispersion with high purity was prepared by an improved Hummer method through a low-temperature reaction process.[43] Typically, this reaction solution is configured according to the ratio of adding 0.1 mmol of sodium ascorbate per 2 mg of GO dispersion, after stirring for about 5 minutes, and the mixture was put into a sealed 15 ml glass vial and reacted at 95 °C for 2 h to fabricate a three-dimensional reduction graphene oxide (3DG) hydrogel. Subsequently, the resulting hydrogel underwent a nitrogen-doping process through a hydrothermal method in ammonia solution. After being washed with deionized water, the 3DNG aerogel was acquired through the freeze-drying method by keeping temperature at −55 °C and vacuum under 100 mTorr.

### 2.2 Preparation of ALDVO@3DNG

The deposition was performed by using a Savannah 100 Atomic Layer Deposition system (Cambridge Nanotech, MA 02142 USA). Before the atomic layer deposition process, the 3DNG should be treated with oxygen plasma. $V_2O_5$ layers were deposited on the electrodes using vanadium triisopropoxy oxide (VTIP) as the reactant at 150 °C for 30, 100, and 200 cycles. These composites were defined as *x*-ALDVO@3DNG, $x = 30$, 100, 200, respectively. According to the files from the manufacturer, each cycle can theoretically add 0.06 nm on the vanadium pentoxide layers. And another sample was prepared by instilling 50 ml vanadium sol (25 mM) into 3DNG, and then freeze dried, and denoted as

TVO@3DNG. And the specific program for the growth of $V_2O_5$ is shown in Fig. S1.†

### 2.3 Preparation of the blank electrolyte and $Li_2S_6$ catholyte

The blank electrolyte was a precisely configured liquid mixture of 1,2-dimethoxyethane (DME) and 1,3-dioxolane (DOL) (1 : 1 ratio by volume) with 1 M lithium bis(trifluoromethanesulfonyl) imide (LiTFSI) and 1 wt% $LiNO_3$ as solutes. The sublimed sulfur powder and $Li_2S$ at a molar ratio of 5 : 1 were added into the blank electrolyte prepared in advance and homogenized by vigorous stirring at 70 °C for 48 hours to obtain the $Li_2S_6$ catholyte.

### 2.4 Adsorption test

In this study, $Li_2S_6$ was adopted as the representative of LiPSs to simplify the experiments and we prepared the $Li_2S_6$ solution with a concentration of 0.005 M. Before the LiPS adsorption test, all 3DG, 3DNG and 100-ALDVO@3DNG and TVO@3DNG were dried at 70 °C for about 12 h. After the LiPS adsorption test for the first time, the containers were sealed in an argon-filled glove box.

### 2.5 Materials characterization

Scanning electron microscopic (SEM) images were collected using a JEOL JSM-7100F. X-ray diffraction (XRD) measurements were carried out to perform crystallographic structural analysis of electrodes on a D8 Advance X-ray diffractometer. Transmission Electron Microscopy (TEM) was performed using a Titan G2 60-300, which can also provide energy dispersive X-ray spectrometer (EDS) images. Raman spectra as well as X-ray photoelectron spectra (XPS) were acquired by using a Renishaw Raman spectroscopy system and VG MultiLab 2000 instrument, respectively. The $V_2O_5$ content was tested by employing a Netzsch STA 449C simultaneous thermogravimetric analyzer (TGA).

### 2.6 Electrochemical measurement

The obtained ALDVO@3DNG cathodes were assembled into CR2025 coin cells, while the anode is lithium metal foil. The reactive substance sulfur was contained in the $Li_2S_6$ catholyte. And all cells were firstly tested at 0.2C for 3 cycles if the current rate was over 0.5C. An Autolab PGSTAT302N was used to get cycle voltammetry (CV) profiles in 1.6–2.7 V (*vs.* $Li/Li^+$) at a scan rate of 0.1 mV $s^{-1}$. All the specific capacities were calculated according to the mass of active S, which was decided by the volume of the catholyte added in the ALDVO@3DNG cathode. The cathode after cycling was gently cleaned with blank DME/DOL solvent and naturally dried at room temperature in an Ar-filled glovebox to avoid oxidation, and then was transferred into a sealed container and prepared for the subsequent characterization.

## 3. Results and discussion

The procedure for fabricating the 3DNG cathodes and the proposed formation mechanism of the $V_2O_5$ nano-level modified layer through atomic layer deposition are schematically illustrated in Fig. 1. First, graphene oxide (GO) sheets were self-assembled into a three-dimensional reduced GO (3DG) hydrogel. Then, nitrogen doping and oxygen plasma treatment were carried out to improve the internal hydrophilicity, which is critical for the ALD process.[32] Finally, $V_2O_5$ was deposited onto the electrodes on both external and internal surfaces uniformly *via* the ALD process.

According to the mechanism of atomic layer deposition, the hydrophilicity of the surface becomes the key point to influence the precision and conditions of the deposition. But the 3DG

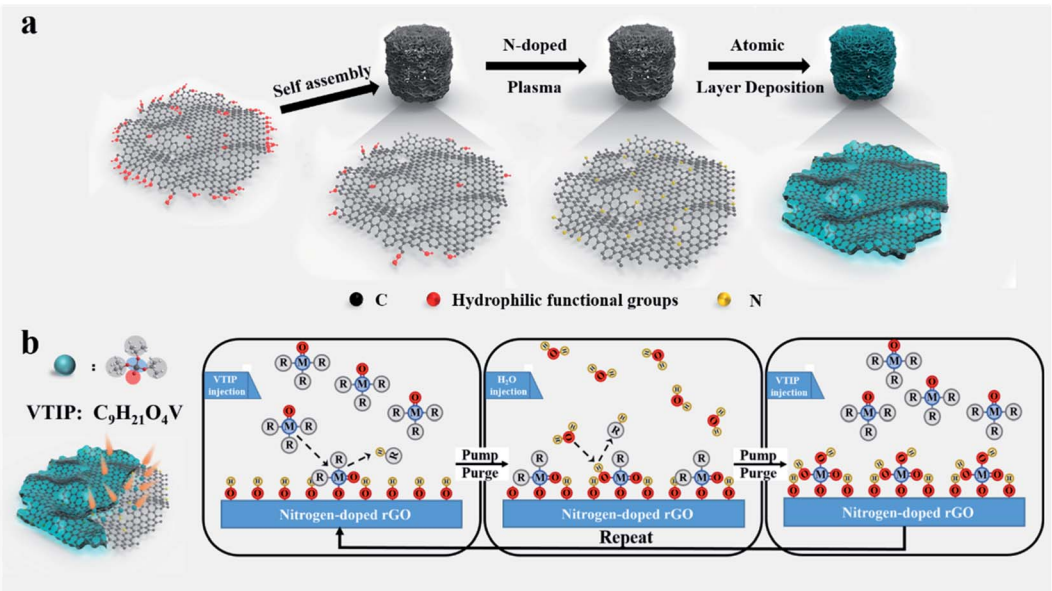


Fig. 1 (a) Schematic of the fabrication of the 3DNG/$V_2O_5$ composite; (b) schematic illustration of the process of atomic layer deposition of $V_2O_5$.

 

possesses a super-hydrophobic external surface after freeze drying, which causes some trouble in deposition, so we try to enhance its hydrophilicity by nitrogen doping[44,45] as well as plasma dispose and the results of contact angle tests are shown in Fig. S2.† In general, the samples can be treated with plasma in air atmosphere to obtain hydrophilicity. This is because the excitation of oxygen, water and carbon dioxide is able to build hydrophilic groups on the surface of the carbon material substrate, such as hydroxyl and carboxyl groups.[46] These photographs exhibit that the surface modified by plasma possesses the best wettability, while the drip nearly doesn't spread out on 3DG and the N-doping method is able to moderately help promote its hydrophilicity. That's why we choose 3DNG with plasma enhanced as the matrix, aiming at smooth deposition both external and internal 3DNG.

### 3.1 Structural characterization

The SEM images of the 100-ALDVO@3DNG electrode are shown in Fig. 2a and b. These pictures show that the 100-ALDVO@3DNG composite has a 3D interconnected network structure with a large number of micron-grade cavities, which can effectively inhibit the S volume expansion problem during charge/discharge and provide larger interspace to carry sufficient sulfur up to high sulfur mass loading. Moreover, the interconnected channel structure becomes the key factor that realizes the uniform deposition of $V_2O_5$, while another one is the hydrophilicity of surfaces. The thickness of deposited $V_2O_5$ is really thin that there is nearly no obvious morphology change on the rGO sheets. This is really different from the SEM image of the sample TVO@3DNG as shown in Fig. S3,† having vanadium oxide laminar material wrapped on the surface of graphene nanosheets, which will severely influence the transport of electrons between LiPSs and the graphene matrix. The TEM images of 100-ALDVO@3DNG are shown in Fig. 2c and its elemental mappings of V and O (Fig. 2d–f) clearly show that element V is distributed on both sides of graphene nanosheets even forming a pattern similar to the tube in the wrinkle areas in Fig. 2d. Besides the close combination between $V_2O_5$ and 3DNG, the ultrathin thickness of $V_2O_5$ that is below 10 nm makes electrons smoothly pass through it. Moreover, further TEM and elemental mapping images of random sheets ultrasonically stripped from 100-ALDVO@3DNG are shown in Fig. S4.† These pictures demonstrate that deposited $V_2O_5$ layers *via* the ALD process indeed cover uniformly in the graphene framework. What's more, linear analysis of the cross section of 100-ALDVO@3DNG (Fig. S5a†) can further verify that decorated materials are successfully deposited in this electrode and develop not only the shallow part of the surface, but also the deep part. We took a HRTEM image of 100-ALDVO@3DNG on a spread graphene surface (Fig. S6a and b†) and it shows distinct lattice fringes with a lattice of 1.99 Å, being consistent with the (411) plane of highly crystallized $V_2O_5$. Besides, the result corresponds to the SEAD pattern shown in Fig. S6c,† which is a typical multiple crystalline diffraction pattern also including the diffraction rings of the 3DNG matrix, while the outermost diffraction ring represents the $V_2O_5$ sample.

The XRD results of the 100-ALDVO@3DNG electrode are shown in Fig. 3a, which is tested on a silicon matrix in order to weaken the influence of 3DNG itself, demonstrating that the $V_2O_5$ deposited through the ALD process corresponds well to $V_2O_5$ (JCPDS card no. 00-001-0359). A comparison of XRD curves of other samples is shown in Fig. S7,† from which we can find that as the content of $V_2O_5$ increases in the sample, the peak envelope intensity of carbon gradually decreases and the characteristic peaks of $V_2O_5$ become more obvious. In Fig. 3b, the Raman spectra of 100-ALDVO@3DNG and TVO@3DNG display similar signatures besides two prominent peaks around 1350 and 1600 $cm^{-1}$ corresponding to the D peak ($sp^3$ hybrid carbon) and G peak ($sp^2$ hybrid carbon). In the 200–1000 $cm^{-1}$ range of the Raman spectra, these two samples display characteristic peaks near 277, 401, 472, 513, 688, and 988 $cm^{-1}$, showing the specific V–O stretches.[47] The chemical valence of ALD deposited $V_2O_5$ was explored by XPS measurements. The V 2p spectrum with V 2p 1/2 at 517.2 eV and V 2p 3/2 at 524.9 eV is consistent

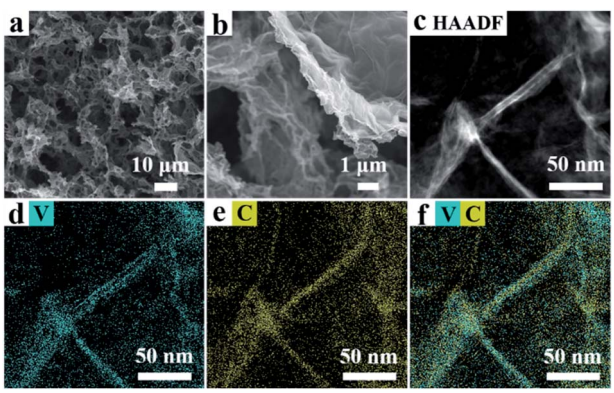


Fig. 2 Morphology and structural characterization of 100-ALDVO@3DNG. (a and b) SEM images; (c–f) local TEM image and elemental mapping images.

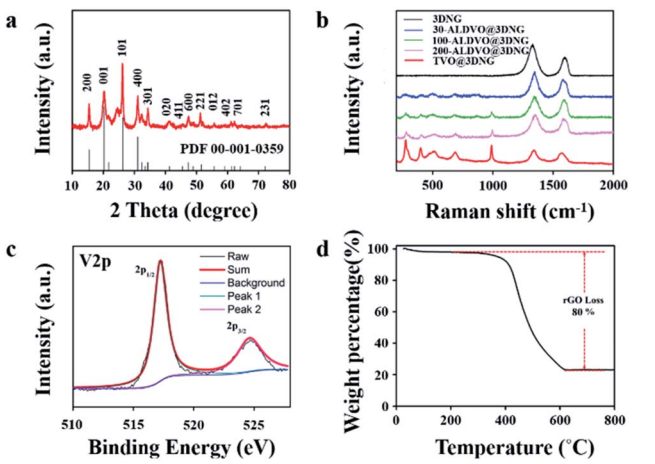


Fig. 3 (a) XRD pattern of the 100-ALDVO@3DNG cathode, (b) Raman spectra of 3DNG, 30-ALDVO@3DNG, 100-ALDVO@3DNG, 200-ALDVO@3DNG and TVO@3DNG, (c) XPS spectra of the ALDVO@3DNG composite, and (d) TG curve of the 100-ALDVO@3DNG composite.

with the +5 valence state of vanadium without other oxidation states (Fig. 3c). According to the TGA results, there exists 20% mass percentage in 100-ALDVO@3DNG (Fig. 3d); this number will then drop to 10.5% after adding the active substance sulfur. Thus, it's apparent that this mass percentage of $V_2O_5$ will further decrease after injecting the $Li_2S_6$ catholyte while assembling cells, which can improve the energy density of the whole device because of less metal oxide adsorption additives.

### 3.2 The electrochemical performance of ALDVO@3DNG cathodes

Fig. 4a shows the foremost four cycles of CV profiles belonging to the 100-ALDVO@3DNG cathode, and there are no obvious peak shifts and current changes, which can provide evidence for the good reversibility of such an electrochemical device with ALDVO@3DNG in limited cycles. This CV curve has two obvious segregated reduction peaks and one overlapped oxidation peak. The two reduction peaks of the first cycle are located at 2.27 and 1.99 V, respectively, being consistent with the electrochemical transformation of LiPSs in Li–S batteries. At 2.27 V, the long-chain LiPSs are converted to short-chain LiPSs, and then further reduced to insoluble discharging products $Li_2S_2/Li_2S$. Beyond that, when the voltage reaches 2.52 V in the charge stage, the oxidation peak is due to the conversion from $Li_2S$ to $Li_2S_8$ and further to $S_8$.[8,48] Reduction peaks show a positive shift while the oxidation peak shows a negative shift, which all indicate improved polysulfide redox kinetics.

The results of assessing the cycling performance of 3DNG, 100-ALDVO@3DNG and TVO@3DNG at 0.2C in galvanostatic cycling from 1.6 to 2.7 V are displayed in Fig. 4b with a sulfur loading of 3.26 mg $cm^{-2}$. 100-ALDVO@3DNG exhibited a capacity of 1555 mA h $g^{-1}$, and after 100 repeated electrochemical cycles, it could still retain 1342 mA h $g^{-1}$ with a retention rate of 86.3%, exhibiting a stable cycling performance. As for the control group, 3DNG delivered an initial capacity of 1530 mA h $g^{-1}$, while TVO-3DNG delivered 1416 mA h $g^{-1}$, and those of these two cathodes severally decreased to 842 mA h $g^{-1}$ and 1090 mA h $g^{-1}$ after 100 cycles. The fact that 100-ALDVO@3DNG and 3DNG cathodes had similar high initial capacity, much higher than that of the TVO@3DNG electrode, demonstrate that excessive $V_2O_5$ with poor conductivity in the electrode would reduce the initial capacity resulting in low energy density of the whole cell, although it can also provide a relatively stable cycle performance because of its good adsorption for LiPSs.

Thus, it is necessary to find out a moderate thickness of ALD deposited $V_2O_5$ layer that is able to provide a stabilized cycling performance without reducing its discharge capacity because the content of $V_2O_5$ in this cathode is too high. Fig. 4c shows the test results of electrodes with different ALD cycles at 0.5C. We can find that the 100-ALDVO@3DNG cathode reaches a relatively high capacity of 1256 mA h $g^{-1}$, and then maintains 1102 mA h $g^{-1}$ after cycling with 0.12% decay per cycle at 0.5C. The 30-ALDVO@3DNG cathode has worse electrochemical performance because its ratio of $V_2O_5$ is too low to support an effective adsorption of LiPSs, while the $V_2O_5$ in 200-ALDVO@3DNG is too much to keep smooth electron transportation between graphene and LiPSs, resulting in low active material utilization and low capacity.

As demonstrated in Fig. 4d, the rate capability of 100-ALDVO@3DNG, 3DNG and TVO@3DNG cathodes was measured at different current rates from 0.2 to 5C. The 100-ALDVO@3DNG cathode could still achieve high capacities of 924, 692, 477 and 195 mA h $g^{-1}$ at 1, 2, 3 and 5C, respectively. Furthermore, while the current rate reversed from 5C to 0.2C, the discharge capacity could recover to 1100 mA h $g^{-1}$ again, illustrating that the 100-ALDVO@3DNG composite electrode had a good electrochemical stability and reversibility. As a comparison, the TVO@3DNG electrode showed lower discharge capacities of 646, 232, 115 and 37 mA h $g^{-1}$, respectively, displaying worse rate capability than 100-ALDVO@3DNG. These results are attributed to the fact that the uniform ultrathin adsorbent *via* moderate cycles of the ALD process is able to enhance the rate capability of cathode, compared with those with superfluous metal oxide modification materials.

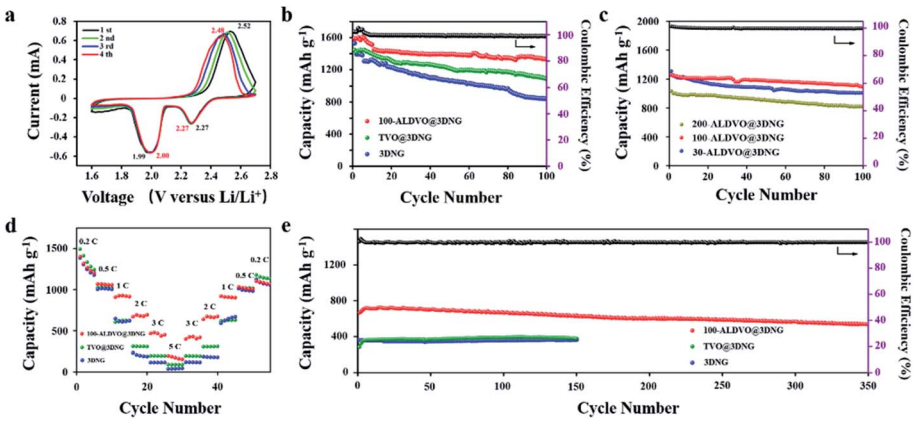


Fig. 4 Electrochemical performances of 3DNG, ALDVO@3DNG and TVO@3DNG cathodes. (a) CV profiles of 100-ALDVO@3DNG at a scan rate of 0.1 mV $s^{-1}$, (b) cycling performance of the 3DNG, 100-ALDVO@3DNG and TVO@3DNG cathodes at 0.2C for 100 cycles, (c) cycling performance of the 30-ALDVO@3DNG, 100-ALDVO@3DNG and 200-ALDVO@3DNG cathodes at 0.5C for 100 cycles, (d) rate performance of the100-ALDVO@3DNG electrode, and (e) cycling stability of the 100-ALDVO@3DNG cathode at 2C for 350 cycles.

 

In Fig. 4e, the long-term cycling performance of 100-ALDVO@3DNG, 3DNG and TVO@3DNG was tested for 350 cycles at 2C. It's evident that the long-term cycling stability of the cathode 100-ALDVO@3DNG was better than that of 3DNG and TVO@3DNG. Typically, the first discharge capability of the 100-ALDVO@3DNG electrode was 664 mA h $g^{-1}$ with gradual increase up to 726 mA h $g^{-1}$. After going through a consecutive 350 cycle test, the 100-ALDVO@3DNG cathode still maintained 542 mA h $g^{-1}$, which corresponds to a capacity retention of 81.6% and a capacity decay of 0.053% per cycle.

In order to bring Li–S batteries closer to commercial applications, a high areal sulfur loading has been a necessary factor on the basis of high theoretical capacity of Li–S batteries.[49] Nevertheless, as the insulated sulfur content in the cathode increases, it will bring about much more severe shuttling of LiPSs as well as worse utilization of active materials, resulting in a rapid capacity decline and lower energy density of the whole device. Thus, it's still difficult to realize a useful performance for cathodes with a high sulfur content rate.[50,51] In this work, in order to further confirm the superiority of the uniform ultrathin adsorbent material decorated cathodes, the cycle performance of 100-ALDVO@3DNG with high S loadings of 6.7 mg $cm^{-2}$ and 11.5 mg $cm^{-2}$ was determined at 0.2C, as displayed in Fig. 5a. The electrode with a sulfur loading of 6.7 mg $cm^{-2}$ delivered a high areal capacity of 9.5 mA h $cm^{-2}$ (1413 mA h $g^{-1}$) after several cycles of activation and retained 7.1 mA h $cm^{-2}$ (1054 mA h $g^{-1}$) after 100 cycles. Besides that, even when the areal S loading was added up to 11.5 mg $cm^{-2}$, the 100-ALDVO@3DNG electrode could still obtain an ultra-high initial capacity of 14.9 mA h $cm^{-2}$ (1296 mA h $g^{-1}$), maintaining 11.2 mA h $cm^{-2}$ (969 mA h $g^{-1}$) after 100 cycles (Fig. 5b). To illustrate the advantages of this work in ALD, we make Table S1†[32–34,37,38] with electrochemical performance comparison of various ALD processes applied in Li–S battery studies. And we further make Fig. 5c which shows that all these numerical data are higher than 4 mA h $cm^{-2}$, which is the standard of practical LiBs, to demonstrate the advantages of 100-ALDVO@3DNG electrode with a high sulfur loading more visibly. Capacities related to the ALD process applied in Li–S batteries recently are shown in Fig. 5d and Table S2.†[52–65] After summarizing these data, the 100-ALDVO@3DNG electrode can reach this high areal capacity maybe attributed to three main characteristics. Firstly, the interconnected network structure with a large number of micro-sized holes can provide a large space to load a mass of sulfur as well as quick transfer passageways for ions and electrons. Secondly, the uniformly deposited $V_2O_5$ covers every point on the surface of the graphene sheets, having more active adsorption sites than a simple mechanically mixed matrix with modificatory materials. Thirdly, the thickness of the $V_2O_5$ nanolayer is so filmy that it will not obviously influence the normal transportation of ions and electrodes although it has a weak conductivity, so it can further improve the transformation rate of LiPSs.

Fig. 6a shows the camera images of the adsorption experiment. 3DNG (NO. 2), TVO@3DNG (NO. 3), 30-ALDVO@3DNG (NO. 4) and 100-ALDVO@3DNG (NO. 5) were immersed into the $Li_2S_6$ catholyte with a concentration of 0.005 M. It's obvious that the color of the electrolyte containing 100-ALDVO@3DNG and TVO@3DNG disappears rapidly after one day with other samples still keeping their yellowish-brown color. And the electrolyte color of 100-ALDVO@3DNG and TVO@3DNG are still keeping clear even after one month of continuous adsorption tests, while the color of solution containing 3DNG and 30-ALDVO@3DNG change a little after one week, even do not become fully clarified after one month, which demonstrates that this two samples have worse adsorption ability to $Li_2S_6$ because of the lack of adequate adsorbent.

In order to further evaluate the adsorption characteristics of the 100-ALDVO@3DNG cathode, we conducted TEM characterization after 100 cycles at 0.5C. It shows that the interconnected network structure still keeps steady (Fig. 6b). And

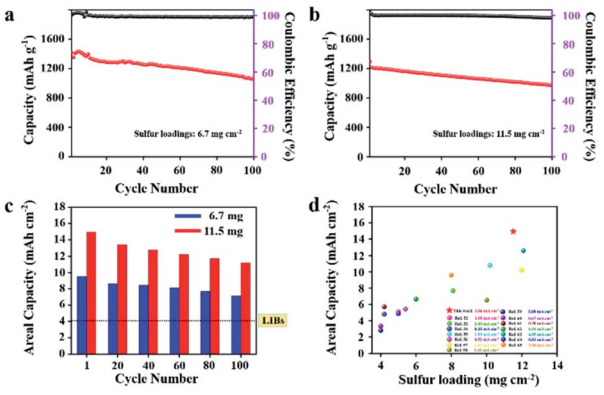


Fig. 5 Cycling performance and the corresponding coulombic efficiency of the 100-ALD@3DNG cathode with (a) 6.7 mg $cm^{-2}$ and (b) 11.5 mg $cm^{-2}$sulfur loadings. (c) Areal capacities of the two electrodes with different sulfur loadings in different cycles. (d) Comparison of the initial areal capacity of this work with that of Li–S batteries from recent publications which were cycled more than 50 times with sulfur loadings higher than 4 mg $cm^{-2}$.

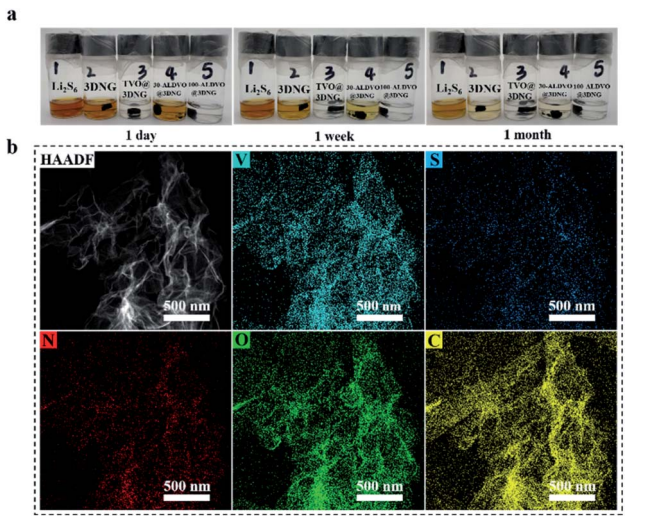


Fig. 6 (a) Optical photograph of the adsorption test for 3DNG, TVO@3DNG, 30-ALDVO@3DNG and 100-ALDVO@3DNG from left to right, respectively; (b) TEM images and elemental mapping images of 100-ALDVO@3DNG after cycling at 0.5C for 100 cycles.

the typical elemental mappings of V, N, O, C and S all exhibit homogeneous distributions in the 100-ALDVO@3DNG framework, from which the large dense clusters of sulfur are not observed. It provides more evidence to demonstrate that the moderate thickness of the uniform $V_2O_5$ layer brings about a higher utilization of sulfur. While adsorbing a large amount of sulfur, the ultrathin $V_2O_5$ decorated layer can also allow it to efficiently diffuse to various positions for reaction, and no bulk accumulation of sulfur is formed, establishing better conductivity. As a consequence, it will make much more sulfur to obtain electrons and ions for reaction from the beginning to the end, leading to a better electrochemical performance.

## 4. Conclusions

In summary, we presented high conductive 3DNG porous interconnected networks decorated with ultrathin polar $V_2O_5$ coatings *via* the ALD technique for lithium sulfur battery cathodes. The highly controllable deposited ultra-thin $V_2O_5$ nanolayers uniformly cover the inner and outer graphene surfaces of 3DNG, which will not significantly affect the conductivity of the ALDVO@3DNG cathode material. This unique design idea can not only effectively suppress the shuttle effect due to its strong chemisorption, but also enable the firmly adsorbed LIPSs to successfully obtain electrons passing through the ultra-thin $V_2O_5$ nanolayers from the graphene matrix. In this way, the utilization efficiency of sulfur is greatly improved, thereby enhancing the cycle performance and rate capability of the batteries, although the conductivity of $V_2O_5$ is not good. A high initial capacity of 1555 and 1256 mA h $g^{-1}$ is obtained at 0.2C and 0.5C, respectively, overcoming the limitation of low initial capacity restricted by the insulating nature of $V_2O_5$, and 86.3% and 87.7% capacity retention are obtained after 100 cycles. The cathode also displays high cycling stability at 2C with a superior capacity recession of 0.052% per cycle. More importantly, the ALDVO@3DNG composite can still achieve a high areal capacity of 14.9 mA h $cm^{-2}$ (1296 mA h $g^{-1}$) with a sulfur mass loading of 11.5 mg $cm^{-2}$. Above all, our work provides a promising approach to suppress the shuttle effects of LiPSs to enable more stable Li–S batteries using a delicate design as well as a new train of thought for ALD application in Li–S batteries.

## Conflicts of interest

There are no conflicts to declare.

## Acknowledgements

This work was supported by the National Natural Science Foundation of China (51702247).

## Notes and references

1 P. G. Bruce, S. A. Freunberger, L. J. Hardwick and J. M. Tarascon, *Nat. Mater.*, 2011, **11**, 19–29.
2 X. Ji, K. T. Lee and L. F. Nazar, *Nat. Mater.*, 2009, **8**, 500–506.
3 H.-J. Peng, J.-Q. Huang, X.-B. Cheng and Q. Zhang, *Adv. Energy Mater.*, 2017, **7**, 1700260.
4 K. Zhu, C. Wang, Z. Chi, F. Ke, Y. Yang, A. Wang, W. Wang and L. Miao, *Front. Energy Res.*, 2019, **7**, 00123.
5 Q. Zhao, X. Hu, K. Zhang, N. Zhang, Y. Hu and J. Chen, *Nano Lett.*, 2015, **15**, 721–726.
6 H. Wang, Y. Yang, Y. Liang, J. T. Robinson, Y. Li, A. Jackson, Y. Cui and H. Dai, *Nano Lett.*, 2011, **11**, 2644–2647.
7 L. Ji, M. Rao, H. Zheng, L. Zhang, Y. Li, W. Duan, J. Guo, E. J. Cairns and Y. Zhang, *J. Am. Chem. Soc.*, 2011, **133**, 18522–18525.
8 Y. X. Yin, S. Xin, Y. G. Guo and L. J. Wan, *Angew. Chem., Int. Ed.*, 2013, **52**, 13186–13200.
9 J. Zhang, C. P. Yang, Y. X. Yin, L. J. Wan and Y. G. Guo, *Adv. Mater.*, 2016, **28**, 9539–9544.
10 X. Liu, J. Q. Huang, Q. Zhang and L. Mai, *Adv. Mater.*, 2017, **29**, 1601759.
11 L. Sun, D. Wang, Y. Luo, K. Wang, W. Kong, Y. Wu, L. Zhang, K. Jiang, Q. Li, Y. Zhang, J. Wang and S. Fan, *ACS Nano*, 2016, **10**, 1300–1308.
12 W. Xue, D. Yu, L. Suo, C. Wang, Z. Wang, G. Xu, X. Xiao, M. Ge, M. Ko, Y. Chen, L. Qie, Z. Zhu, A. S. Helal, W.-K. Lee and J. Li, *Matter*, 2019, **1**, 1047–1060.
13 M. Li, Y. Zhang, X. Wang, W. Ahn, G. Jiang, K. Feng, G. Lui and Z. Chen, *Adv. Funct. Mater.*, 2016, **26**, 8408–8417.
14 L. Lin, F. Pei, J. Peng, A. Fu, J. Cui, X. Fang and N. Zheng, *Nano Energy*, 2018, **54**, 50–58.
15 X. Liang, Y. Rangom, C. Y. Kwok, Q. Pang and L. F. Nazar, *Adv. Mater.*, 2016, **29**, 201603040.
16 J. Schuster, G. He, B. Mandlmeier, T. Yim, K. T. Lee, T. Bein and L. F. Nazar, *Angew. Chem., Int. Ed.*, 2012, **51**, 3591–3595.
17 G. Li, J. Sun, W. Hou, S. Jiang, Y. Huang and J. Geng, *Nat. Commun.*, 2016, **7**, 10601.
18 Y. Chen, S. Choi, D. Su, X. Gao and G. Wang, *Nano Energy*, 2018, **47**, 331–339.
19 S. Lu, Y. Cheng, X. Wu and J. Liu, *Nano Lett.*, 2013, **13**, 2485–2489.
20 M. Yu, R. Li, Y. Tong, Y. Li, C. Li, J.-D. Hong and G. Shi, *J. Mater. Chem. A*, 2015, **3**, 9609–9615.
21 Z. Li, Q. He, X. Xu, Y. Zhao, X. Liu, C. Zhou, D. Ai, L. Xia and L. Mai, *Adv. Mater.*, 2018, **30**, 1804089.
22 W. Xue, Z. Shi, L. Suo, C. Wang, Z. Wang, H. Wang, K. P. So, A. Maurano, D. Yu and Y. Chen, *Nat. Energy*, 2019, **4**, 374–382.
23 J. Nelson, S. Misra, Y. Yang, A. Jackson, Y. Liu, H. Wang, H. Dai, J. C. Andrews, Y. Cui and M. F. Toney, *J. Am. Chem. Soc.*, 2012, **134**, 6337–6343.
24 Z. Wang, Y. Dong, H. Li, Z. Zhao, H. B. Wu, C. Hao, S. Liu, J. Qiu and X. W. Lou, *Nat. Commun.*, 2014, **5**, 5002.
25 Z. Li, J. Zhang and X. W. Lou, *Angew. Chem., Int. Ed.*, 2015, **54**, 12886–12890.
26 Z. Zhang, Y. Lai, Z. Zhang, K. Zhang and J. Li, *Electrochim. Acta*, 2014, **129**, 55–61.
27 W. Li, G. Zheng, Y. Yang, Z. W. Seh, N. Liu and Y. Cui, *Proc. Natl. Acad. Sci. U. S. A.*, 2013, **110**, 7148–7153.

 

28 F. Liu, Q. Xiao, H. B. Wu, F. Sun, X. Liu, F. Li, Z. Le, L. Shen, G. Wang, M. Cai and Y. Lu, *ACS Nano*, 2017, **11**, 2697–2705.
29 X. Liang, C. Y. Kwok, F. Lodi-Marzano, Q. Pang, M. Cuisinier, H. Huang, C. J. Hart, D. Houtarde, K. Kaup, H. Sommer, T. Brezesinski, J. Janek and L. F. Nazar, *Adv. Energy Mater.*, 2016, **6**, 1501636.
30 M. Q. Zhao, C. E. Ren, Z. Ling, M. R. Lukatskaya, C. Zhang, K. L. Van Aken, M. W. Barsoum and Y. Gogotsi, *Adv. Mater.*, 2015, **27**, 339–345.
31 M. Naguib, O. Mashtalir, M. R. Lukatskaya, B. Dyatkin, C. Zhang, V. Presser, Y. Gogotsi and M. W. Barsoum, *Chem. Commun.*, 2014, **50**, 7420–7423.
32 F. Sun, J. Wang, D. Long, W. Qiao, L. Ling, C. Lv and R. Cai, *J. Mater. Chem. A*, 2013, **1**, 13283.
33 Z. Li, J. Zhang, B. Guan, D. Wang, L. M. Liu and X. W. Lou, *Nat. Commun.*, 2016, **7**, 13065.
34 B. Yan, X. Li, Z. Bai, X. Song, D. Xiong, M. Zhao, D. Li and S. Lu, *J. Power Sources*, 2017, **338**, 34–48.
35 J. Zhang, G. Zhang, Z. Chen, H. Dai, Q. Hu, S. Liao and S. Sun, *Energy Storage Mater.*, 2019, **26**, 513–533.
36 H. Kim, J. T. Lee, D.-C. Lee, A. Magasinski, W.-i. Cho and G. Yushin, *Adv. Energy Mater.*, 2013, **3**, 1308–1315.
37 M. Yu, W. Yuan, C. Li, J.-D. Hong and G. Shi, *J. Mater. Chem. A*, 2014, **2**, 7360–7366.
38 M. Yu, A. Wang, F. Tian, H. Song, Y. Wang, C. Li, J. D. Hong and G. Shi, *Nanoscale*, 2015, **7**, 5292–5298.
39 Y. S. Jung, A. S. Cavanagh, L. Gedvilas, N. E. Widjonarko, I. D. Scott, S.-H. Lee, G.-H. Kim, S. M. George and A. C. Dillon, *Adv. Energy Mater.*, 2012, **2**, 1022–1027.
40 E. Memarzadeh Lotfabad, P. Kalisvaart, K. Cui, A. Kohandehghan, M. Kupsta, B. Olsen and D. Mitlin, *Phys. Chem. Chem. Phys.*, 2013, **15**, 13646–13657.
41 M. Yu, J. Ma, H. Song, A. Wang, F. Tian, Y. Wang, H. Qiu and R. Wang, *Energy Environ. Sci.*, 2016, **9**, 1495–1503.
42 R. Carter, L. Oakes, N. Muralidharan, A. P. Cohn, A. Douglas and C. L. Pint, *ACS Appl. Mater. Interfaces*, 2017, **9**, 7185–7192.
43 J. W. S. Hummers and R. E. Offeman, *J. Am. Chem. Soc.*, 1958, **80**, 1339.
44 H.-L. Guo, P. Su, X. Kang and S.-K. Ning, *J. Mater. Chem. A*, 2013, **1**, 2248–2255.
45 B. Ouyang, Y. Zhang, Y. Wang, Z. Zhang, H. J. Fan and R. S. Rawat, *J. Mater. Chem. A*, 2016, **4**, 17801–17808.
46 M. Leskelä and M. Ritala, *Thin Solid Films*, 2002, **409**, 138–146.
47 R. Baddour-Hadjean, J. P. Pereira-Ramos, C. Navone and M. Smirnov, *Chem. Mater.*, 2008, **20**, 1916–1923.
48 C. Barchasz, F. Molton, C. Duboc, J. C. Lepretre, S. Patoux and F. Alloin, *Anal. Chem.*, 2012, **84**, 3973–3980.
49 C. Zhang, S.-H. Park, S. E. O'Brien, A. Seral-Ascaso, M. Liang, D. Hanlon, D. Krishnan, A. Crossley, N. McEvoy, J. N. Coleman and V. Nicolosi, *Nano Energy*, 2017, **39**, 151–161.
50 H. Tang, W. Li, L. Pan, C. P. Cullen, Y. Liu, A. Pakdel, D. Long, J. Yang, N. McEvoy, G. S. Duesberg, V. Nicolosi and C. J. Zhang, *Adv. Sci.*, 2018, **5**, 1800502.
51 H. Tang, W. Li, L. Pan, K. Tu, F. Du, T. Qiu, J. Yang, C. P. Cullen, N. McEvoy and C. Zhang, *Adv. Funct. Mater.*, 2019, **29**, 1901907.
52 X. Zhu, W. Zhao, Y. Song, Q. Li, F. Ding, J. Sun, L. Zhang and Z. Liu, *Adv. Energy Mater.*, 2018, **8**, 1800201.
53 M. Yu, J. Ma, M. Xie, H. Song, F. Tian, S. Xu, Y. Zhou, B. Li, D. Wu, H. Qiu and R. Wang, *Adv. Energy Mater.*, 2017, **7**, 1602347.
54 Q. Zhao, Q. Zhu, J. Miao, Z. Guan, H. Liu, R. Chen, Y. An, F. Wu and B. Xu, *ACS Appl. Mater. Interfaces*, 2018, **10**, 10882–10889.
55 Q. Pang, X. Liang, C. Y. Kwok, J. Kulisch and L. F. Nazar, *Adv. Energy Mater.*, 2016, **7**, 1601630.
56 L. Ma, H. Yuan, W. Zhang, G. Zhu, Y. Wang, Y. Hu, P. Zhao, R. Chen, T. Chen, J. Liu, Z. Hu and Z. Jin, *Nano Lett.*, 2017, **17**, 7839–7846.
57 P. Han, S. H. Chung, C. H. Chang and A. Manthiram, *ACS Appl. Mater. Interfaces*, 2019, **11**, 17393–17399.
58 C. Chen, J. Jiang, W. He, W. Lei, Q. Hao and X. Zhang, *Adv. Funct. Mater.*, 2020, **30**, 1909469.
59 C. Zha, D. Wu, T. Zhang, J. Wu and H. Chen, *Energy Storage Mater.*, 2019, **17**, 118–125.
60 Y. T. Liu, D. D. Han, L. Wang, G. R. Li, S. Liu and X. P. Gao, *Adv. Energy Mater.*, 2019, **9**, 1803477.
61 R. Zhuang, S. Yao, M. Liu, J. Wu, X. Shen and T. Li, *Int. J. Energy Res.*, 2019, **43**, 7655–7663.
62 P. Han, S.-H. Chung and A. Manthiram, *Energy Storage Mater.*, 2019, **17**, 317–324.
63 Y. Peng, Z. Wen, C. Liu, J. Zeng, Y. Wang and J. Zhao, *ACS Appl. Mater. Interfaces*, 2019, **11**, 6986–6994.
64 M. Zensich, T. Jaumann, G. M. Morales, L. Giebeler, C. A. Barbero and J. Balach, *Electrochim. Acta*, 2019, **296**, 243–250.
65 J. Shi, Q. Kang, Y. Mi and Q. Xiao, *Electrochim. Acta*, 2019, **324**, 134849.